Nuclear Instruments and Methods in Physics Research A 654 (2011) 546–559

Contents lists available at ScienceDirect

Nuclear Instruments and Methods in Physics Research A

journal homepage: www.elsevier.com/locate/nima

The AX-PET demonstrator—Design, construction and characterization

P. Beltrame [a], E. Bolle [g], A. Braem [a], C. Casella [b,*], E. Chesi [e], N. Clinthorne [f], R. De Leo [d], G. Dissertori [b], L. Djambazov [b], V. Fanti [a,1], M. Heller [a], C. Joram [a], H. Kagan [e], W. Lustermann [b], F. Meddi [h], E. Nappi [d], F. Nessi-Tedaldi [b], J.F. Oliver [c], F. Pauss [b], M. Rafecas [c], D. Renker [b,2], A. Rudge [e], D. Schinzel [b,3], T. Schneider [a], J. Séguinot [e], P. Solevi [c], S. Stapnes [g], P. Weilhammer [e]

[a] *CERN, PH Department, CH-1211 Geneva, Switzerland*
[b] *Institute for Particle Physics, ETH Zurich, CH-8093 Zurich, Switzerland*
[c] *IFIC (Universidad de Valencia/CSIC), E-46071 Valencia, Spain*
[d] *INFN, Sezione di Bari, I-70122 Bari, Italy*
[e] *Ohio State University, Columbus, Ohio 43210, USA*
[f] *University of Michigan, Ann Arbor, MI 48109, USA*
[g] *University of Oslo, NO-0317 Oslo, Norway*
[h] *University of Rome "La Sapienza", I-00185 Rome, Italy*

ARTICLE INFO

Article history:
Received 12 April 2011
Received in revised form
7 June 2011
Accepted 9 June 2011
Available online 17 June 2011

Keywords:
PET
Axial geometry
Geiger-mode Avalanche Photo Diodes
(G-APD)
SiPM

ABSTRACT

Axial PET is a novel geometrical concept for Positron Emission Tomography (PET), based on layers of long scintillating crystals axially aligned with the bore axis. The axial coordinate is obtained from arrays of wavelength shifting (WLS) plastic strips placed orthogonally to the crystals. This article describes the design, construction and performance evaluation of a demonstrator set-up which consists of two identical detector modules, used in coincidence. Each module comprises 48 LYSO crystals of 100 mm length and 156 WLS strips. Crystals and strips are readout by Geiger-mode Avalanche Photo Diodes (G-APDs). The signals from the two modules are processed by fully analog front-end electronics and recorded in coincidence by a VME-based data acquisition system. Measurements with point-like ^{22}Na sources, with the modules used both individually and in coincidence mode, allowed for a complete performance evaluation up to the focal plane reconstruction of point sources. The results obtained are in good agreement with expectations and proved the set-up to be ready for the next evaluation phase with PET phantoms filled with radiotracers.

1. Introduction

Positron Emission Tomography is a powerful but also complex functional medical imaging method. It is based on the recording of the two coincident 511 keV photons following the annihilation of a positron, emitted from a radiotracer. Tomographic reconstruction of the coincidence data allows for 3D reconstruction of the source distribution.

More than 50 years of research and development have been aimed at improved spatial resolution and sensitivity of the PET scanner. Fast, high-Z and high density scintillators, together with the increased sensitivity and speed of new photodetectors and the improvements in their readout electronics, allowed substantial progress in terms of background suppression (random coincidences) and data acquisition capabilities (count-rate saturation). Equally important are the progresses achieved in the treatment of the acquired data, using advanced statistical reconstruction methods, accounting for sampling inhomogeneities and compensating for image-degradation phenomena, such as attenuation, scattering in the object, etc.

The physics of PET, in particular the diffusion of the positron in the tissue prior to annihilation and the small non-collinearity of the two annihilation photons, pose some constraints on the highest achievable spatial resolution, which depends on the scanner diameter and on the radioisotope. These phenomena can be partially compensated for by including an adequate model of both positron range and acollinearity into a statistical iterative reconstruction algorithm. In this way, spatial resolution values at the millimeter level could be achieved. A clinical realization of such an ultimate performance with a full-body system requires also compensation for patient motion [1].

The standard PET geometry is based on the radial arrangement of scintillating crystals, readout at one end by a photodetector.

---

[*] Corresponding author.
E-mail address: Chiara.Casella@cern.ch (C. Casella).
[1] Now at Università e Sezione INFN di Cagliari, Italy.
[2] Now at Technical University München, 85748 Garching, Germany.
[3] Now at Laboratory for Nuclear Science, Massachussetts Institute of Technology, Cambridge 02139-4307, USA.

0168-9002/$ - see front matter © 2011 Elsevier B.V. All rights reserved.
doi:10.1016/j.nima.2011.06.059

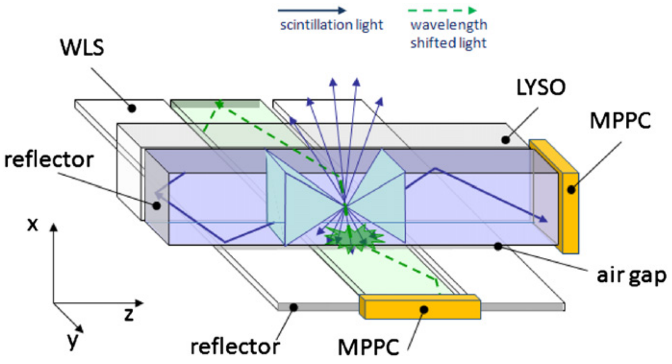

Fig. 1. Principle of the light propagation in the scintillating crystal and the WLS strips.

To keep the number of readout channels manageable, blocks of crystals are often readout together, by means of Anger logic. Absent or limited depth-of-interaction information leads to the parallax error, resulting in a degradation of the spatial resolution, which deteriorates toward the peripheral region of the field of view. Reducing the length of the crystals mitigates the problem but also compromises the sensitivity of the system.

The axial concept, which we demonstrate in a fully operational set-up consisting of two camera modules, avoids the compromise between resolution and sensitivity, and allows to tune both, independently from each other. The physical spatial resolution limits are in reach while high sensitivity can be maintained. Although not part of this report, it is still worth mentioning that the axial concept does not preclude in any way the use of Time-Of-Flight information or the coregistration of PET with a magnetic resonant system (MRI).

1.1. The Axial PET concept

The main characteristic of the Axial PET (AX-PET) [2] is the axial arrangement of long and individually read scintillating crystals. The crystals, stacked in several layers, are aligned parallel to the axis of the scanner (Z-axis). The address of the hit crystal yields the 2D spatial information (X,Y) of the photons interaction point with a resolution determined by the cross-section of the crystal.[4] The third coordinate (Z) is derived from layers of wavelength shifting (WLS) plastic strips, which are placed, with a small air gap, below each crystal layer in the perpendicular direction (Fig. 1). Both the crystals and the strips are readout individually by Geiger-mode Avalanche Photo Diodes (G-APD) on one side, while the other end is covered by a thin reflective Aluminum coating. G-APDs, also known as SiPMs (Silicon Photo Multipliers), will be referred in the text as MPPCs (Multi Pixel Photon Counters).

Following the energy deposition, a correlated quantity of scintillation light is isotropically emitted in a crystal. Light which is emitted inside the cone of the total reflection travels inside the crystal and is collected by the MPPC, providing the energy measurement. The fraction of the light which lies outside the cone escapes from the crystal and is absorbed by the WLS strips. After wavelength conversion (from blue to green), a fraction of it travels inside the strips toward the photodetector. The address of the WLS strip gives the Z coordinate. Usually, light is detected by more than one strip and a weighted average can be used to derive the axial coordinate with a precision which exceeds the digital resolution determined by the strip width.

The axial concept leads to a fully unambiguous 3D position reconstruction of the annihilation photons without parallax error. The spatial resolution and the sensitivity of the PET camera module can be tuned independently by varying, respectively, the crystal/strip dimensions and the number of crystal layers. The 3D photon tracking capability of our concept allows the identification of the Compton interactions in the crystal matrix (Inter Crystal Scattering). Simulations suggest that a large fraction of those scattering events can be fully recovered [3].

1.2. Short historical overview

The axial arrangement of the scintillating crystals is a natural and straightforward idea to suppress the parallax error which is inherent to all radial geometries. In 1988, Shimizu et al. [4] described an axial geometry of a PET camera, where a matrix of crystals was readout on both sides by segmented photodetectors. The axial coordinate was proposed to be derived from the ratio of the light levels detected at the two ends of the crystal. The concept was patented but to our knowledge never experimentally proven. A subgroup of the authors of this article worked for several years on the implementation of a similar axial concept using double sided readout with Hybrid Photon Detectors (HPD) specifically developed for this purpose [5,6]. However, an axial resolution in the millimeter range remained an unachieved goal. The excellent optical transparency of state-of-the-art scintillating crystals, which optimizes energy and time resolution, is obviously counterproductive for the light sharing. The well-proven concept of reading scintillators via wavelength shifters together with the advent of a novel type of photodetector, the MPPC, allowed to conceive a new implementation of the axial concept which overcomes these limitations [7]. The replacement of the vacuum based HPD by the solid state MPPC device brings in addition immunity to magnetic fields which is a prerequisite for the combination of PET and MRI.

1.3. Overview of the article

This article describes the design, the construction and the results of detailed characterization measurements of two identical AX-PET modules, which we consider as a demonstrator set-up for the concept. The article is organized as follows. Section 2 describes the geometry of the modules and the main properties of all their essential components and readout. This is followed by a description in Section 3 of the experimental set-up and analysis strategy adopted for the measurements. The results of the characterization measurements are given in Sections 4 and 5, respectively, for modules performance and coincidence measurements. Finally, in Section 6, we conclude and give an outlook on measurements with PET phantoms.

2. The AX-PET module

Each AX-PET module consists of six layers of eight crystals and 26 WLS strips each, hence a total of 48 scintillator crystals and 156 WLS strips (see Fig. 2). Crystals and strips are readout by two different types of MPPCs. Each MPPC is individually supplied and adjusted to a constant gain according to temperature variations. The signals are amplified and processed by a dedicated VLSI-ASIC in order to obtain a precise measurement of the collected charge, proportional to the energy deposition in the crystals and to the light yield in the WLS strips. A trigger logic allows to set a lower and an upper threshold on the total energy deposition in the whole module (e.g. 400 and 600 keV). The data is readout via a

---

[4] $\sigma_{X,Y} = d/\sqrt{12}$ where d is the transverse dimension of the crystal.

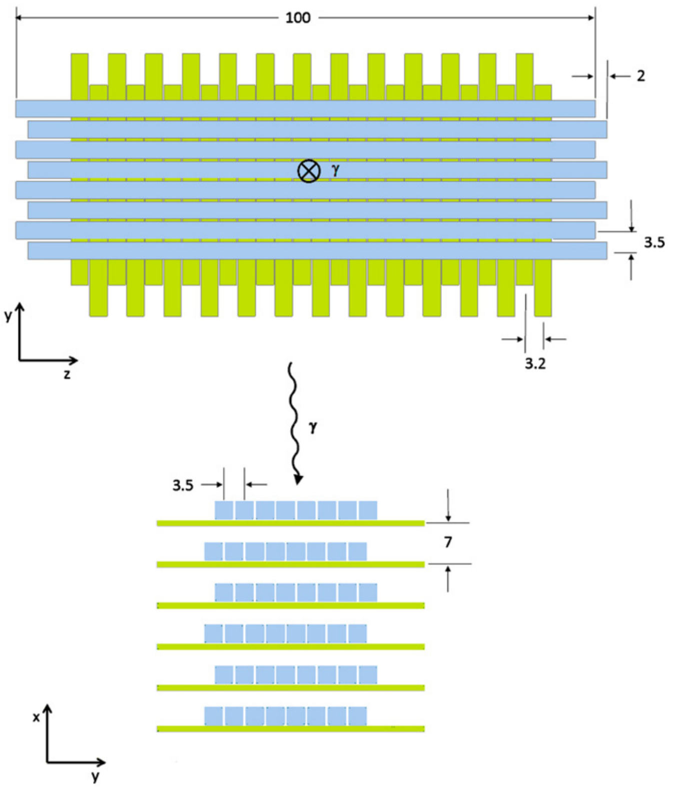

Fig. 2. Two-side views of the geometry of each AX-PET module. The distances are expressed in mm.

VME-PC interface into a standard desktop computer. The details of these components are described in the following subsections.

2.1. *The scintillating crystal bars*

The scintillating bars are made of LYSO crystals ($Lu_{1.8}Y_{0.2}$-SiO_5:Ce), produced by Saint-Gobain[5] (marketed as PreLudeTM 420). LYSO is a non-hygroscopic scintillator material, with the following properties: density $\rho = 7.1\ \mathrm{g/cm^3}$; light yield $LY = 32$ photons/keV; temperature dependence of the light yield $d(LY)/dT = -0.2\%/\mathrm{K}$; attenuation length (at 511 keV) $\lambda_{511} = 12$ mm; scintillation decay time $\tau = 42$ ns, in a single exponential. The emission spectrum of LYSO extends from 360 to 600 nm with the peak emission at 420 nm. LYSO contains a naturally radioactive β emitter isotope, ^{176}Lu, which decays predominantly to the excited state of ^{176}Hf (597 keV); the latter decays to the ground state with a three gamma cascade of energies 307, 202 and 88 keV. The emission of the three gammas is simultaneous with the β emission. The intrinsic activity is 39 cps/g.

The LYSO crystals used for the AX-PET demonstrator have the dimensions $3 \times 3 \times 100\ \mathrm{mm^3}$. All surfaces are optically polished, the edges are sharp and crack-free. The crystals are used without any wrapping or coating, except for the non-readout face opposite to the MPPC, which is coated with a reflective (80–85%) Aluminum film of typically 100 nm thickness. Prior to coating, all crystals were individually characterized in terms of their intrinsic energy resolution and effective optical absorption length (λ^*_{opt}) in a dedicated set-up.[6] The results obtained show that $\lambda^*_{opt} = (412 \pm 31)$ mm and $(\Delta E/E)_{intr} = (8.3 \pm 0.5)\%$ (FWHM) at 511 keV [8].

2.2. *The wavelength shifting strips*

The wavelength shifting (WLS) plastic strips are of type EJ-280-10x from Eljen Technology.[7] Their dimensions are $3 \times 0.9 \times 40\ \mathrm{mm^3}$. They are based on Polyvinyltoluene (PVT) and have on request a 10 times higher dye concentration than the EJ-280 standard product. The high dye concentration leads to an absorption length for blue light of about 0.4 mm (see Fig. 3). Hence, the strip thickness of 0.9 mm corresponds to more than two absorption lengths. The absorption maximum matches well the emission spectrum of LYSO. The non-read end of the WLS strip is coated with a reflective Aluminum film of typically 100 nm thickness with a reflectivity of the order 70–80%. A sub-set of the WLS strips have been characterized in a dedicated set-up. The effective optical absorption length for the wavelength shifted light was found to be $(\lambda^*_{opt})_{WLS} = (188 \pm 36)$ mm, prior to the coating with the Al film [9].

2.3. *The photodetectors*

The LYSO crystals and the WLS strips are individually readout by fast Geiger-mode Avalanche Photo Diodes (G-APD) from Hamamatsu,[8] marketed as MPPC: Multi Pixel Photon Counters. The MPPCs used for the crystals are of type S10362-33-050C, with a $3 \times 3\ \mathrm{mm^2}$ active area, subdivided in 3600 cells of size $50 \times 50\ \mu\mathrm{m^2}$. The MPPCs are mounted on a ceramic carrier and the photo-sensitive surface is protected with a hard epoxy resin. For the readout of the WLS strips, custom tailored MPPCs of $3.22 \times 1.19\ \mathrm{mm^2}$ active area, subdivided in 782 cells of $70 \times 70\ \mu\mathrm{m^2}$ size, are used. These MPPCs are mounted on an octagon-shaped substrate with the same epoxy protection. The MPPCs are glued to the LYSO crystal bars or WLS strips with the optically transparent silicone Dow Corning(R) 3145 RTV. The alignment with the sensitive area of the MPPC and their gluing is assured by a dedicated tool.

The entire set of MPPCs used for the crystals and a subsampling of the MPPCs used for the WLS strips were characterized to determine the bias voltage for a fixed charge gain. The gain value is chosen to optimize the photon detection efficiency (PDE $\sim 40\%$), keeping the dark noise and optical cross-talk at an acceptable level. The parameters are summarized in Table 1.

Each of the 408 MPPCs is biased independently. The bias is provided by a custom built control unit [10], based on commercial AD5535 32-channel voltage 14 bit DACs. The unit is driven by a LabVIEW[9] program, which reads the required voltage settings from a master table. In order to maintain a stable MPPC gain, the master table is corrected according to the measured temperature variation ($dG/dT \sim -4.8\%/\mathrm{K}$, see Section 4.8).

2.4. *Mechanical design*

The mechanical design of the camera module is driven by several partly conflicting requirements: highest possible packing density (compatible with the commercially available MPPC packages); positioning precision of all the active elements at the 0.1 mm level; minimum optical contact between the structural and the active elements to preserve light collection efficiency; a reasonably low material budget to minimize the Compton

---

[5] Saint-Gobain Cristaux, 77794 Nemours, France.

[6] The effective optical absorption length describes the absorption of the scintillation photons while propagating along the crystal, including the multiple

(*footnote continued*)
bouncing due to reflections at the surfaces. Projected on the *Z*-axis, λ^*_{opt} is shorter than the bulk optical absorption length.

[7] Eljen Technology, Sweetwater Texas 79556, United States.

[8] Hamamatsu Photonics K.K., Japan.

[9] From National Instruments, http://www.ni.com/labview.

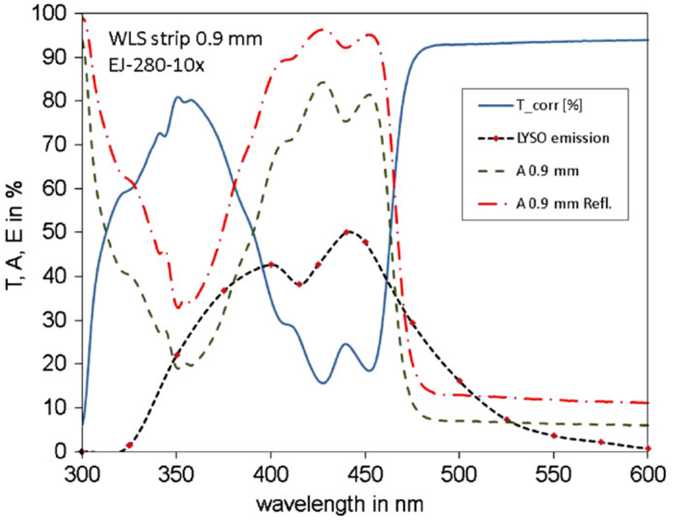

Fig. 3. Measured light transmission (solid line) through one WLS strip. The data taken with an industrial spectrophotometer is corrected for the Fresnel reflections at the strip entrance. The other curves show the measured emission spectrum of LYSO (line with data points) and the absorption of a 0.9 mm thick strip, with and without reflection from a mirror (R=0.8) mounted behind the strip.

Table 1
Main characteristics and operational parameters of the MPPCs. Gain, bias and noise rates refer to a temperature of 25 °C. V_{bias} reports the mean bias value and its RMS, averaged over 96 crystal MPPCs and 312 WLS MPPCs.

	Crystal MPPC	WLS MPPC
Type	S10362-33-050c	Custom tailored
Charge gain G	6×10^5	1×10^6
V_{bias}	(70.95 ± 0.22) V	(70.38 ± 0.59) V
dG/dV	$55 \times 10^4\ \mathrm{V}^{-1}$	$110 \times 10^4\ \mathrm{V}^{-1}$
Noise rate at 0.5 pe	4.7 MHz	3.2 MHz
Noise rate at 1.5 pe	0.9 MHz	0.5 MHz

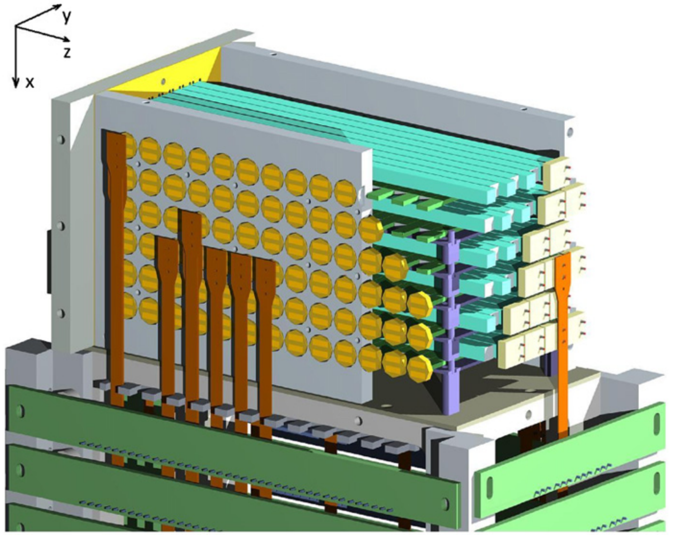

Fig. 4. Mechanics of an AX-PET camera module. Some components, like the light tight cover and some structural components, have been removed for better clarity.

scattering; last but not least, ease of disassembly in view of possible repairs or replacements.

Figs. 2 and 4 show the mechanical assembling of one AX-PET module, with the LYSO crystals arranged in six layers of eight crystals each. To maximize the packing density, crystals and WLS strips are readout on alternate sides. The crystal pitch in a layer is 3.5 mm, the layer-to-layer pitch in the X direction is 7 mm. The eight crystals in one layer are axially staggered in the Z coordinate by 2 mm. The crystal layers are staggered in the Y coordinate by half the crystal pitch (1.75 mm). This staggering among layers serves to optimize the photon interaction probability. A set of 26 WLS strips is mounted underneath each crystal layer with an air gap in the X coordinate of 0.2 mm. The WLS strip pitch is 3.2 mm. The WLS strips are staggered by 5.4 mm in Y, but there is no horizontal staggering between WLS strips of different layers. The six layers of crystals and WLS strips are optically separated by thin carbon fiber sheets (not shown in the figures) which are painted with white diffuse reflector paint on the side facing the WLS. They avoid propagation of scintillation light from one layer to the next and increase the effective light absorption in the WLS strips.

The crystals are held in place by two thin perforated masks, consisting of photolithographically produced CuBe sheets which minimize the mechanical contact to a few points. The assembly is fixed inside an Aluminum box structure which also supports the MPPCs on the front and side panels. In the axial direction, the MPPCs push the crystals slightly against foam stoppers. The WLS strips are held in place by the MPPCs to which they are glued. An auxiliary framestructure, partly visible in the bottom part of Fig. 4, is attached to the module in order to mount patch panels which transmit bias voltage and signal pulses. The entire module structure is contained in a light tight Aluminum box; the entry window for photons is a 50 μm thin Aluminum foil.

2.5. Front end electronics

The AX-PET demonstrator features fully analog readout electronics for the 96 crystals and 312 WLS strips. The front-end electronics amplifies the signals from the photodetectors and transfers them to VATAGP5 ASIC chips [11]. The signals are integrated with a 300 ns shaping time by the ASIC and, in case of a positive trigger decision, digitized by a 10-bit ADC. In order to minimize the on-detector electronics, for reasons of heat dissipation and lack of space, the MPPC signals are distributed to patch panels via kapton strip-line cables. They are then transmitted via thin coaxial cables to custom made amplifier PCB boards, care being taken to minimize time of flight variations between the detector elements.

The functionality of one channel is shown schematically in Fig. 5. The general architecture of the front-end and DAQ system is sketched in Fig. 6. The MPPC output signals are sent to 50 Ω input impedance voltage amplifiers, with a gain of 7.5 for the LYSO and of 50 for the WLS signals. Texas Instruments[10] amplifiers OPA843 and OPA847 (Gain bandwidth product 3.9 GHz), respectively, are used. A sum of the total energy deposited in each module is generated from the LYSO amplifiers and used in the external trigger to select 511 keV events (see Section 2.7). The summed LYSO signal is DC coupled from the MPPCs, to avoid rate induced baseline shifts.

The amplifier outputs provide a current input via to four VATAGP5 chips, mounted on separate PCBs. The VATAGP5 chip can be used either in serial readout mode, by multiplexing all channels, or in sparse readout mode, by addressing only the hit channels above threshold. At the input, signals are splitted into two branches, a fast and a slow one. The fast branch consists of a 50 ns shaper followed by a discriminator. Signals above a chosen threshold are stored in a hit register. Following a trigger, a data lock signal enables the register for a duration of 60 ns and the selected channels are then readout via the slow 300 ns shaper.

---

[10] Texas Instruments, http://www.ti.com.

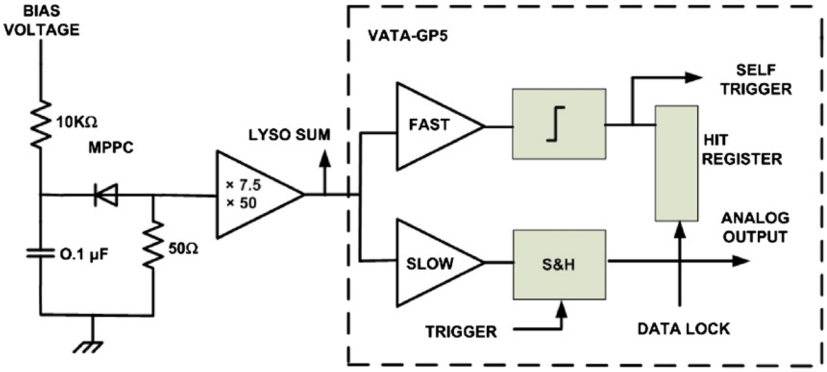

Fig. 5. Simplified representation of the functionality of one electronic channel.

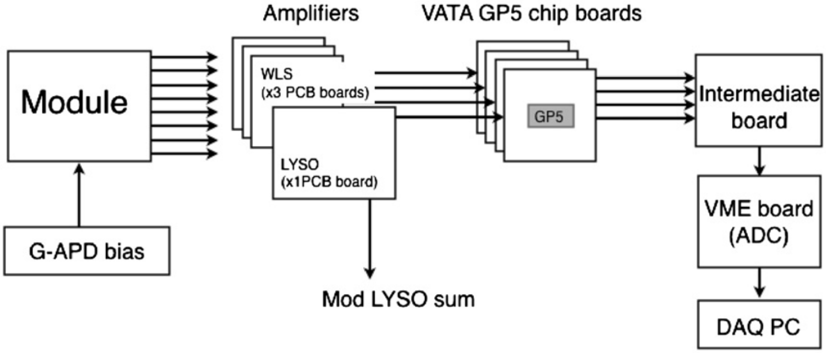

Fig. 6. Schematics of the front-end and DAQ architecture for the readout of one module.

Their analog output is then readout via the 10-bit ADC in the data acquisition system.

The trigger signal can be provided either externally or internally (self-triggering mode). When the internal trigger is used, any of the channels above threshold starts the acquisition. Normally data taking is performed with the external trigger. The internal trigger is used to detect the intrinsic radioactivity of the LYSO crystals, useful for the energy calibration. In both trigger options, the sparse readout mode is used. The serial one is only adopted for pedestals acquisition.

2.6. Data acquisition

The data acquisition system makes use of custom made VMEbus boards based on XILINX FPGA. One VME board controls one module and receives the signals from an intermediate board which synchronizes the signals of the four VATAGP5 chips used for the module (Fig. 6).

The DAQ software runs on a MEN[11] A20 single board processor installed in the VME crate. It also communicates with a slow control PC at the beginning of each run of data taking through the DIM[12] protocol. The communication is used to read the temperature of the module and store it in the data file. It is also used to control the motion system and store the coordinates in the data file, as described below. The system achieves data taking rates in excess of 10 kHz.

2.7. Trigger

A trigger circuit was conceived for the tests with a ^{22}Na source. It exploits the fact that the ^{22}Na isotope decays – with the emission of a positron – to an excited state of Ne. The positron, that has 0.21 MeV average kinetic energy, annihilates at rest with a nearby electron, with the emission of two quasi antiparallel photons, each of 511 keV energy. The daughter nucleus ^{22}Ne* decays, within picoseconds of the positron emission, to its ground state with the emission of a photon of 1.27 MeV energy.

The trigger circuit forms coincidences, either between the two AX-PET modules or between one module and a small tagging scintillator, used for testing purposes. The circuit – implemented with standard NIM modules – is shown in Fig. 7. The pulse height LYSO sum of each module is discriminated at thresholds corresponding to about 50 keV (LL), 400 keV (HL) and 600 keV (HHL). A coincidence of the type $\mathrm{LL} \times \mathrm{HL} \times \overline{\mathrm{HHL}}$ ensures that events are recorded only if the energy detected in one module is in the range 400–600 keV, suppressing the 1.27 MeV gamma photon emitted by the source. The coincidence is such that the discrimination at 50 keV defines the timing of the $\mathrm{LL} \times \mathrm{HL} \times \overline{\mathrm{HHL}}$ signal, thus minimizing its time walk. The use of the sum signal represents a fast and elegant way to decide whether the module detected a 511 keV photon interaction, independently of the details of the interaction in the module (photoelectric effect, Compton plus photoelectric effect, etc.). Depending on the set-up requirements, the coincidence of the two modules $(\mathrm{LL} \times \mathrm{HL} \times \overline{\mathrm{HHL}})_1 \times (\mathrm{LL} \times \mathrm{HL} \times \overline{\mathrm{HHL}})_2$ or the coincidence of one module with the tagger $(\mathrm{LL} \times \mathrm{HL} \times \overline{\mathrm{HHL}})_i \times (\mathrm{LL} \times \overline{\mathrm{HHL}})_{tagger}$ is used as trigger for the DAQ. The tagging crystal is only discriminated twofold, at 50 and 400 keV thresholds. A simple dead time logic also avoids pile-up of events.

2.8. Temperature monitoring

The modules are operated in an air-conditioned room but are not individually cooled. As described in Section 4.8, the gain of the MPPCs shows a strong temperature dependence, which is an order of magnitude larger than the temperature dependence of the light yield of the LYSO crystals. In order to maintain a constant gain, the

---

[11] MEN Mikro Elektronik GmbH, Nuremberg, Germany.

[12] Distributed Information Management, www.cern.ch/DIM.

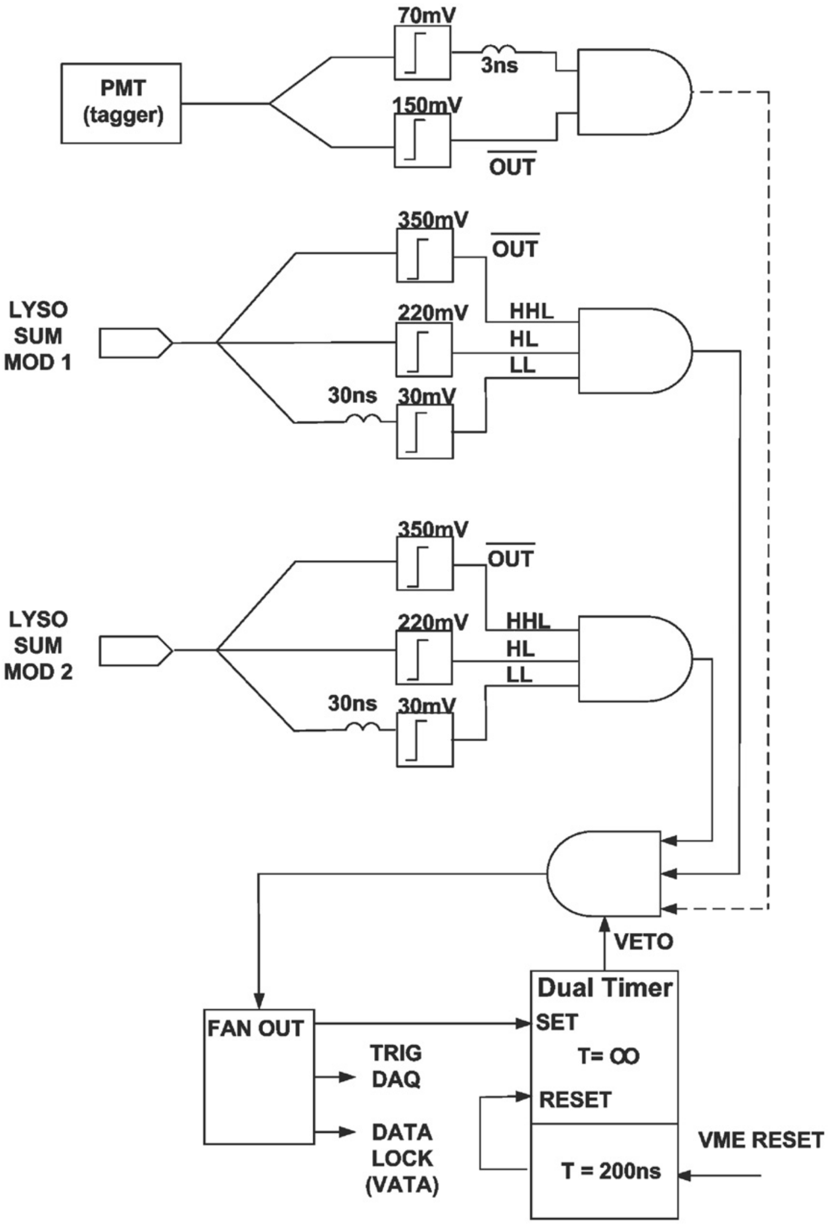

Fig. 7. Schematic representation of the external trigger logic.

MPPCs bias voltage must be changed according to temperature variations. If temperature changes are recorded during the data taking, gain corrections can also be applied in the offline analysis. The temperature is permanently monitored by means of four temperature sensors AD590 from Analogue Devices,[13] placed on the module frame, and recorded by a LabVIEW program. Prior to their installation in the set-up, the sensors have been calibrated over a large temperature range, by the direct comparison with accurate temperature probes inside a small climate chamber. A precision of 0.1 K is achieved with the calibrated temperature sensors.

3. Experimental set-up and analysis

An experimental set-up has been built to scan with a photon beam of controlled dimensions over the surface of the detector modules. This procedure was mainly used for the individual characterization of each module. A small modification of the set-up also allowed for tests with the two modules in coincidence.

3.1. Scanning set-up

The scanning set-up for the single module characterization is shown in Fig. 8. A ^{22}Na radioactive source is used. The source (activity 1 MBq, active diameter 0.25 mm, embedded in the center of a plexiglass disc of 25.4 mm diameter and 6.35 mm thickness) is mounted between the module and a small scintillating crystal, used to tag the 511 keV photons from the source, by selecting coincidence events between the module and the scintillator. The tagging crystal (LYSO) is read by a fast photomultiplier tube with 8 mm active diameter, from Hamamatsu Photonics, Model R7400U. Two different tagging crystals, of dimensions $2 \times 2 \times 12$ and $2 \times 10 \times 12$ mm^3, are used. Acting on the relative distances between the tagger, the source and the module, different photon beam spot sizes on the module are achieved. Typically, two

---

[13] http://www.analogue.com

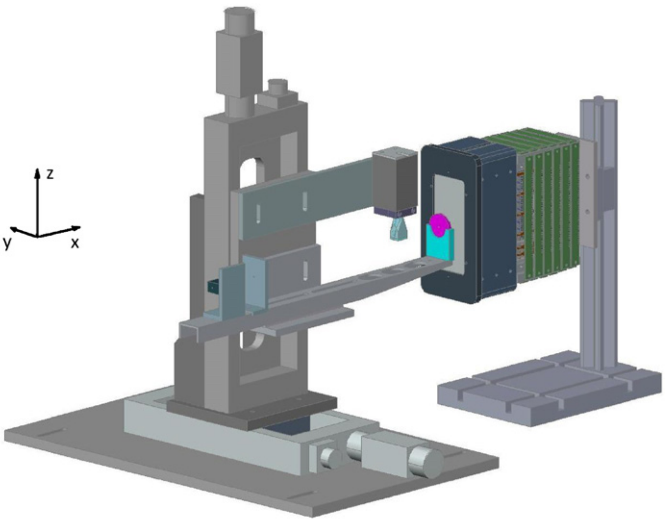

Fig. 8. 3D schematic of the scan set-up.

different configurations are adopted. The first one ("small tagger set-up") uses the smaller crystal as a tagger and the source placed as close as possible to the module; this provides a collimated photon beam of ~0.4 mm RMS on the most external layer. The second arrangement ("big tagger set-up") uses the bigger crystal and the maximum distance between the source and the module to achieve a large spot with a uniform illumination of the module. Typical rates of about 100 and 450 Hz are recorded, respectively, for the small and big tagger set-up. This is in good agreement with the values expected from solid angle and detection probability considerations.

In the set-up the module is kept fixed, while the ^{22}Na source is mounted on a movable two axes (Y and Z) linear motion system, together with the tagger. By displacing the source and tagger system, the full module surface can be scanned with a precision of about 0.1 mm. The two axes are motorized and computer controlled via a LabVIEW interface.

3.2. Coincidence set-up

A simple modification of the scanning set-up allows for measurements with the two modules in coincidence. The two modules are fixed one in front of the other, at 15 cm distance. The ^{22}Na source is mounted in between on the two axes movable system, to study the coincidence response in various axial and transaxial positions. The typical measured coincidence rate is about 3 kHz, with the source in the central position.

3.3. Analysis software

A ROOT [12] based analysis code is applied on the raw data set, acquired by the DAQ system. In sparse readout mode, the ADC values of all the hits above the VATAGP5 threshold are recorded for each triggered event, both for the LYSO and for the WLS signals. The analysis requires a dedicated pedestal run prior to the acquisition, then it performs the pedestal subtraction on a channel by channel basis and – if requested – the correction of the ADC values for temperature variations. The analysis then processes the data to extract all the relevant information i.e. position and energy of every interaction. With this information, different selection cuts are applied and several histograms are filled. Further corrections for LYSO energy calibration and for the optical attenuation length, both in the LYSO and in the WLS strips, can also be included in the analysis as additional options, in particular for Compton events reconstruction.

4. Characterization of single modules

Photoelectric absorption events (i.e. only one LYSO crystal hit per module, with full photon energy deposition) are used to characterize the basic performance of the AX-PET modules in terms of detection efficiency, uniformity and axial resolution. To determine the energy resolution, an energy calibration is performed using both the photoelectric absorption and the intrinsic radioactivity in the LYSO crystals. Additional corrections for the light absorption and for the temperature variation are presented at the end of this section. They provide a further optimization of the module performance and a deeper understanding of the detector. They also become fundamental when Compton scattering events are considered. Approaches to deal with Compton interactions in the crystals and a comparison of the data with a dedicated Monte-Carlo model are the subject of a forthcoming article [14].

4.1. Crystals and WLS response

All multiplicities of LYSO crystals in one module are a priori allowed, provided that the energy sum over the full module fullfills the discrimination requirements of the external trigger. A large fraction of the recorded events (more than 60%) corresponds to events with only one LYSO hit in the module. Given the trigger requirements on the energy, these events represent to a large extent pure primary photoelectric interactions in one of the crystals. This simple cut on the LYSO multiplicity does not prevent a small contamination from soft Compton scattered events. In addition, a Compton interaction followed by the photoelectric absorption of the scattered photon in the same crystal bar would not be distinguished from a primary photoelectric interaction.

Fig. 9 shows the typical energy distribution in one single LYSO bar, both for all the events (photoelectric and Compton interactions) and for the events with LYSO hit multiplicity equal to 1 (photoelectric absorption). The contribution from the Compton scattering almost totally vanishes when the cut on the multiplicity is applied, except for a small low energy tail on the

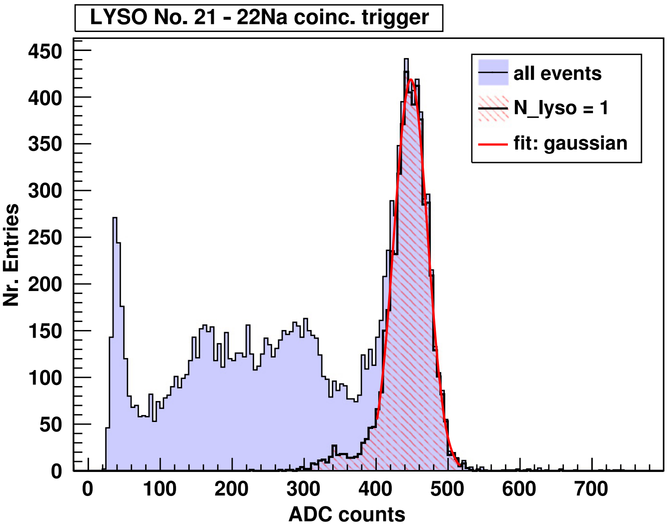

Fig. 9. Charge spectrum of 511 keV photons detected in one LYSO bar, both for all the events (i.e. no cut, solid filled histogram) and for the photoelectric absorption events (N_lyso = 1, striped filled histogram). A Gaussian fit is also applied on the photoelectric peak.

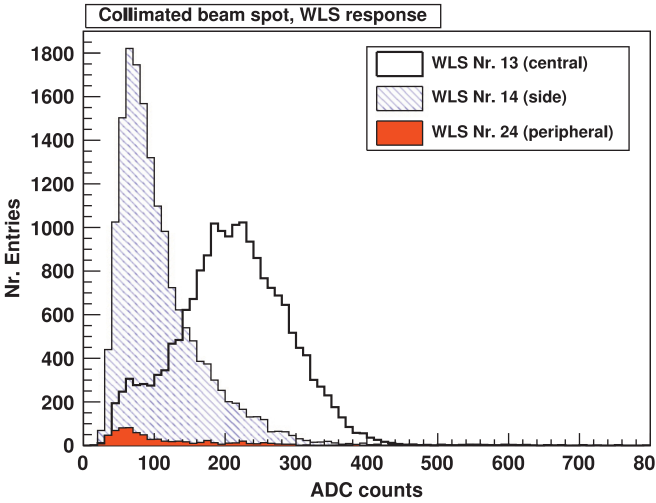

Fig. 10. Detection of 511 keV photons in the WLS strips. The histograms show the charge spectra of three representative WLS strips in the module, for photoelectric absorption events with a collimated beam spot, centered in the middle of WLS no. 13. The considered WLS strips lie on the same layer of the singly detected crystal, in three different axial positions (13, 14, 24).

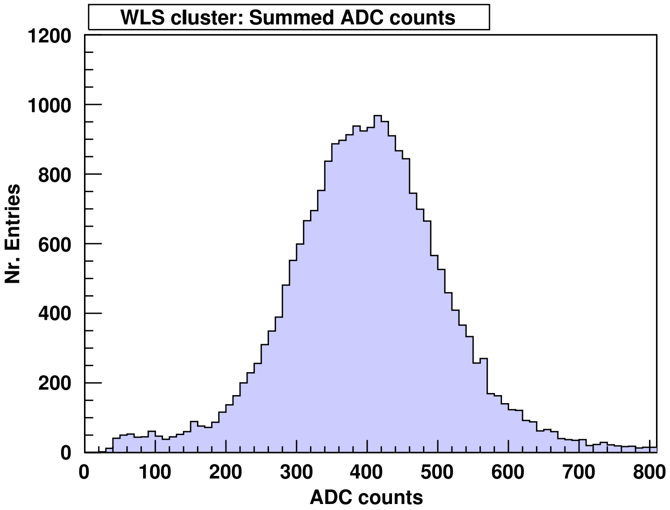

Fig. 11. Summed charge spectrum for all the WLS strips belonging to the WLS cluster, for photoelectric absorption events in the LYSO bars. The average total light yield in the cluster is ~100 photoelectrons.

photopeak. The lowest energy peak in the full energy distribution is the characteristics X-ray emission from the Lu K-shell, corresponding to an energy of about 55 keV [15]. This peak corresponds to photons which accompany the photoelectric absorption process in the LYSO crystals surrounding the considered bar; they escape the crystals from which they are emitted, and are eventually detected by the selected one. The distribution shown in Fig. 9 refers to one randomly selected LYSO crystal in the module, when the module is uniformly exposed to 511 keV photons from the ^{22}Na source (i.e. set-up with the big tagger). The detected spectrum is accurately reproduced by Monte-Carlo data [13]. The accurate Monte-Carlo description will be further demonstrated in Ref. [14].

A collimated beam spot from the set-up with the small tagger is used to characterize the response of the WLS strips. Fig. 10 shows the raw ADC spectra of some representative WLS strips. The strips lie in the same layer of the singly detected LYSO bar for a beam spot collimated in the center of the module and focused in the middle of a WLS strip. For relative comparison, the spectra of three representative WLS strips are shown: the central one (where the beam is, and the maximum of the signal is detected); an adjacent strip on one of the two sides (where a significant part of the signal is still detected); a peripheral strip (where only noise is recorded). A consistent behavior is registered for all the 26 positions of the WLS strips in the layer. To reconstruct the *Z*coordinate, the contribution from the noise must be removed. To do this, a cluster algorithm is applied on all the WLS detected in the same layer of the LYSO crystal. A cluster is defined as a group of adjacent WLS strips above the detection threshold. Only the WLS strips in the cluster are used to compute the reconstructed *Z*coordinate, derived as the weighted average – on an event by event basis – of the axial coordinate of the strips, weighted over the individual strip response. The cluster summed distribution (Fig. 11) contains the information about the total collected light yield for photoelectric events. The cluster algorithm allows for an efficient rejection of the noise, which mainly consists of isolated WLS strips with low ADC values.

The calibration for the WLS strips (i.e. the conversion from ADC counts to number of photoelectrons) is performed with two independent methods: direct injection of a known charge in the readout chain and absolute calibration of the single photoelectron response from the dark noise integrated spectrum. Both methods lead to comparable results of 3–4 ADC counts/photoelectron. From the mean value of the cluster summed distribution of Fig. 11, a global light yield of about 100 photoelectrons in all the WLS involved in the event is achieved. This is valid for the 511 keV photoelectric absorption events and scales linearly with the energy deposition in the crystals, down to a minimum photon energy of about 100 keV. For lower energies photons, the axial coordinate is not anymore reliably reconstructed. The light yield in the cluster is on average shared among three strips. Contrary to the expectations, a linear dependence of the cluster total light yield with the multiplicity of strips in the cluster is observed. The effect – currently under investigation [16] – has, however, a very limited impact on the reconstruction of the *Z* coordinate.

4.2. Detection efficiency and uniformity

For the photoelectric absorption events, the spatial information of the photon interaction point is unambiguously obtained, within the spatial resolutions. The transaxial coordinate (X,Y) is assigned at the center of the crystal in which the full energy deposition is detected. The axial *Z* coordinate is derived from the center of gravity method applied on the WLS strips of the identified cluster. A good uniformity in the target – convoluted with the beam spot size on the module – is achieved, as shown in Fig. 12.

From the statistics of photoelectric events per layer, an approximate measurement of the attenuation length (λ_{511}) in the LYSO matrix can be derived. The result is shown in Fig. 13: the measured value is $\lambda_{511} = (3.973 \pm 0.033)$ layers à 3 mm $=$ (11.9 ± 0.1) mm, in very good agreement with the nominal value from LYSO data sheets. It should be noted that the obtained value of the attenuation length includes contributions of the divergence of the 511 keV photons and the *Y* staggering of the layers which make the effective traversed material thickness vary from one event to the other.

4.3. Axial resolution

The reconstructed *Z* coordinate of photoelectric interactions, measured with the collimated beam set-up (as described in Section 3.1), allows to derive an estimate of the axial resolution. The fitted σ value of the reconstructed *Z* distribution shown in

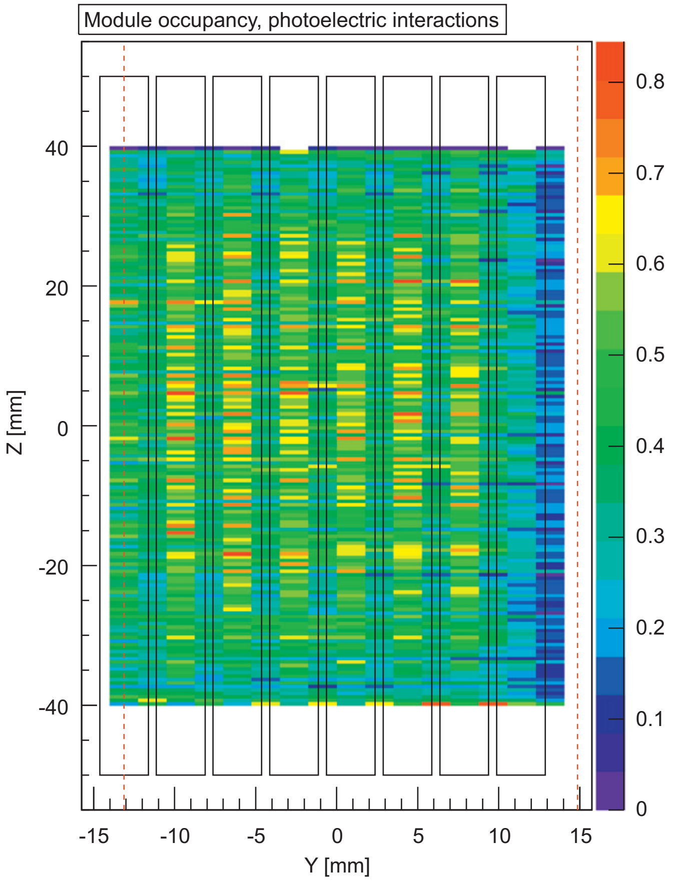

Fig. 12. Projected *YZ* occupancy of photoelectric interactions, with the set-up optimized for a uniform illumination of the module. The drawn rectangular regions represent the LYSO crystals positions in the most external LYSO layer; the dashed red lines define the borders of the second LYSO layer; the staggering of the crystals justifies the chosen binning of 1.75 mm in the *Y* coordinate. In the *Z* coordinate (continuous distribution), an arbitrary bin size of 0.5 mm is chosen. The color scale corresponds to percentage of events over the total statistics. (For interpretation of the references to color in this figure legend, the reader is referred to the web version of this article.)

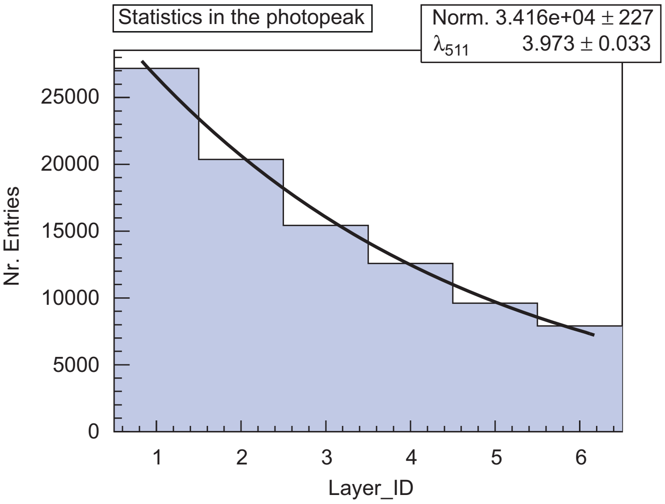

Fig. 13. Statistics of photoelectric events as a function of the layer in which they are detected. The distribution is fitted with an exponential function.

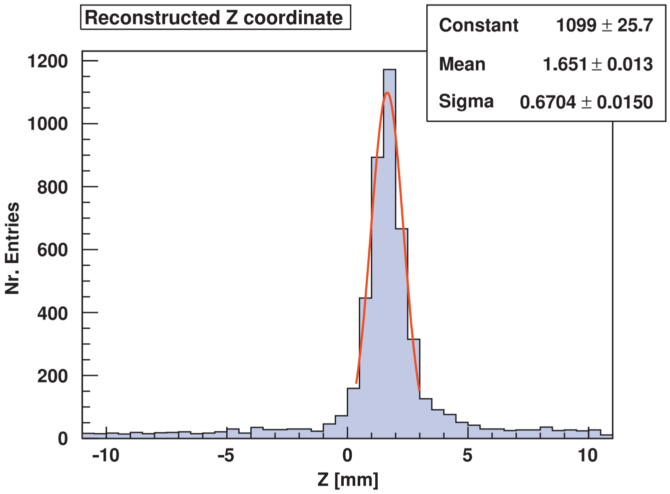

Fig. 14. Reconstructed *Z* coordinate for photoelectric events in the first layer of the module, for a collimated beam in a fixed position of the source scan. The coincidence set-up includes the module and the small tagging crystal; the source is at a distance of 19 mm from the module. The tails in the distribution are accidentals, due to the close distance between module and source. The distribution is fitted with a Gaussian function around its maximum.

Fig. 14 is the convolution of the intrinsic spatial resolution of the detector σ_{intr} and the photon beam spot size σ_{spot}. The latter includes a pure geometrical component σ_{geo}, together with the contributions from the physics of the e^+ annihilation i.e. the finite positron range σ_ρ and the non-collinearity of the two emitted photons σ_{NC}:

$$\sigma = \sqrt{\sigma_{intr}^2 + \sigma_{spot}^2} = \sqrt{\sigma_{intr}^2 + \sigma_{geo}^2 + \sigma_\rho^2 + \sigma_{NC}^2} \tag{1}$$

The σ_ρ value is derived from the FWHM value of 0.54 mm quoted in Ref. [17]: $\sigma_\rho = 0.23$ mm.[14] The non-collinearity of the two photons is described by a Gaussian angular distribution with about 0.5° FWHM width [17]; this leads to a resolution term which scales with the distance d between the source and the detector: $\sigma_{NC} = 0.0037 \cdot d$. Due to the finite size of the tagger, also the geometrical beam spot term scales linearly with the distance from the source. The physical size of the source (0.25 mm diameter) is practically negligible. Following the above considerations, the intrinsic spatial resolution is derived by the fitted σ measurements of the Z coordinate in the six layers, extrapolated to distance $d = 0$. Fig. 15 shows the σ^2 versus d^2 data points, as measured independently on the six layers of the two modules. The increasing in the widths of the reconstructed Z distribution as a function of the distance from the source is explained by the divergency of the beam and the non-collinearity contribution. Eq. (1) justifies the linear interpolation of the σ^2 versus d^2 measurement. The extrapolation to zero distance eliminates both the geometrical and the non-collinearity terms. The square root of the axis intercept still includes the contribution of the intrinsic resolution and the finite positron range. Subtracting in quadrature the σ_ρ term, intrinsic axial resolutions of 1.75 and 1.82 mm (FWHM) are obtained for the two modules.

4.4. Intrinsic radioactivity in the crystals

The intrinsic radioactivity of the LYSO accounts for an activity of about 250 Bq of β decays out of a single $3 \times 3 \times 100\ \text{mm}^3$ crystal bar, corresponding to a rate of about 12 kHz per module. The β emission is accompanied by γ photons. Given the particular geometry of the crystals – with a high surface over volume ratio –

---

[14] The average range of ^{22}Na positrons in plexiglas is assumed to be equal to the average range of the ^{18}F positrons in water, which is commonly reported in the literature, because of the similar average positron energy.

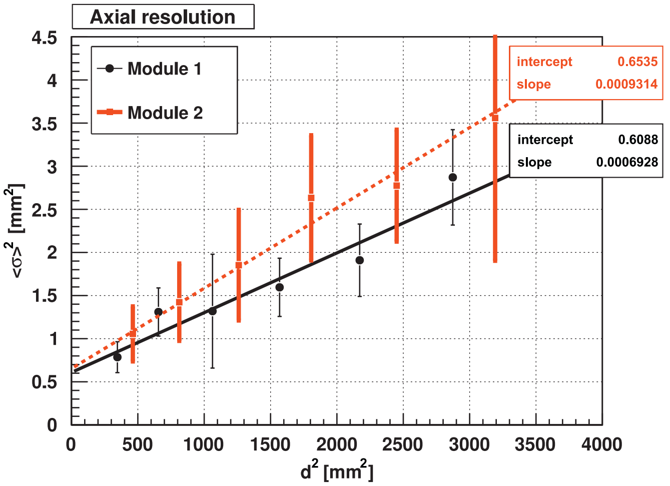

Fig. 15. Axial resolution for 511 keV events, in the set-up with a collimated beam. For each module, the data points correspond to the measured σ of the reconstructed Z distribution in each one of the six layers. Each point is the average over 28 measurements, corresponding to different scanning positions of the tagger in the YZ plane. The difference between the two modules is due to a repositioning of the tagger set-up (increased distance from tagger to module, in case of Module 2).

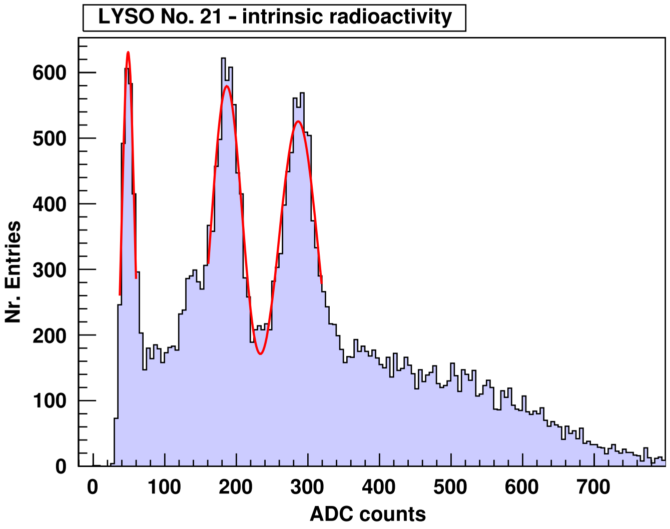

Fig. 16. Intrinsic radioactivity of one LYSO bar: charge spectrum of a single crystal in the module matrix.

and their close assembly in the matrix module, a significant fraction of the photons from the intrinsic radioactivity could escape the crystal bars, and be detected by the neighboring ones. This is not the case for the β particles, which deposit all their energy in the crystal where they are produced. The typical energy spectrum of intrinsic radioactivity for one single LYSO crystal in the module is shown in Fig. 16. The accurate Monte-Carlo description of these data will be demonstrated in Ref. [14]. The continuous distribution in the spectrum represents the intrinsic radioactivity of the bar itself (β's and the trapped γ's), the peaks are due to the γ's produced by the neighboring crystals, which escape them, and are eventually detected in the considered crystal. The two higher energy peaks (202 and 307 keV) correspond to the de-excitation photons from the intrinsic radioactivity. The third photon (88 keV) is not detected, mainly because of its high internal conversion probability [18]. The lowest energy peak is the Lu X-ray peak (55 keV).

As it will be shown, the intrinsic radioactivity of the LYSO crystals is a powerful tool for the energy calibration. Gaussian fits are applied on the peaks, and their positions are extracted. Dedicated runs without the ^{22}Na source and with the readout operated in internal trigger mode are performed to obtain the intrinsic radioactivity spectra.

4.5. Energy calibration of the crystals

The goal of the energy calibration in the crystals (i.e. conversion from ADC counts to energy units) is twofold: the equalization of all the channels in the matrix and the correction for the non-linearity of the MPPCs. Energy calibration is certainly necessary for the reconstruction of Compton scattered events, where a precise energy knowledge is required, but it is also needed to correctly determine the energy resolution.

The energy calibration is performed on a channel by channel basis, using both the intrinsic radioactivity and the external trigger spectra, as shown, respectively, in Figs. 16 and 9. A Gaussian fit of the peaks at known energies – namely the Lu X-ray peak (55 keV), the Lu γ decay lines (202 and 307 keV) and the photopeak (511 keV) – is applied. A curve like the one in Fig. 17 is then derived for each LYSO crystal. At low energies the MPPC response is linear, but it starts to saturate already at energies close to the photopeak. This is due to the limited number of cells combined with the important light yield from the crystal. A deviation from the linearity of about 5% is measured at 511 keV. The ADC versus energy scale is thus parameterized with a 3-parameters fitting function:

$$E(ADC)=p_0-p_1\cdot\ln\left(1-\frac{ADC}{p_2}\right). \tag{2}$$

In order to guarantee optimum energy resolution, the calibration procedure is applied individually to all 96 crystal-MPPC pairs.

4.6. Energy resolution

Good results in terms of crystals energy resolution and uniformity are achieved, as shown in Figs. 18 and 19. Both plots refer to the energy measurements in LYSO after having applied the energy calibration i.e. already corrected for the MPPC non-linearity.

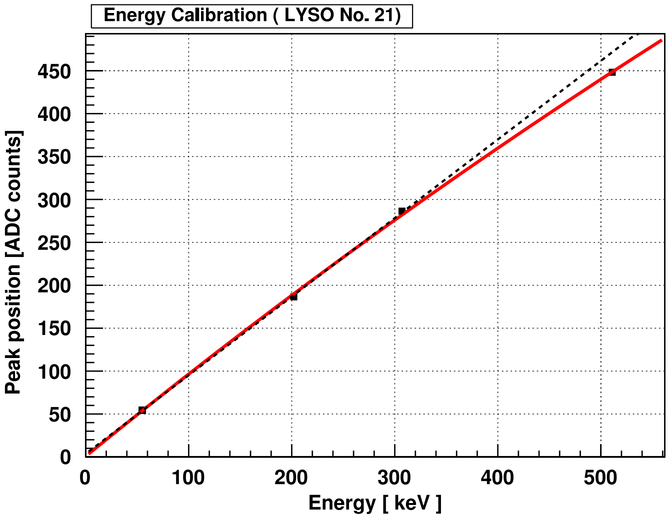

Fig. 17. Energy calibration curve for one LYSO crystal. The plot shows the fitted mean values versus the energies for the peaks of intrinsic radioactivity and the photopeak. The red continuous line represents the fitting curve. Its deviation from linearity (dashed black line) arises from the MPPC saturation. (For interpretation of the references to color in this figure legend, the reader is referred to the web version of this article.)

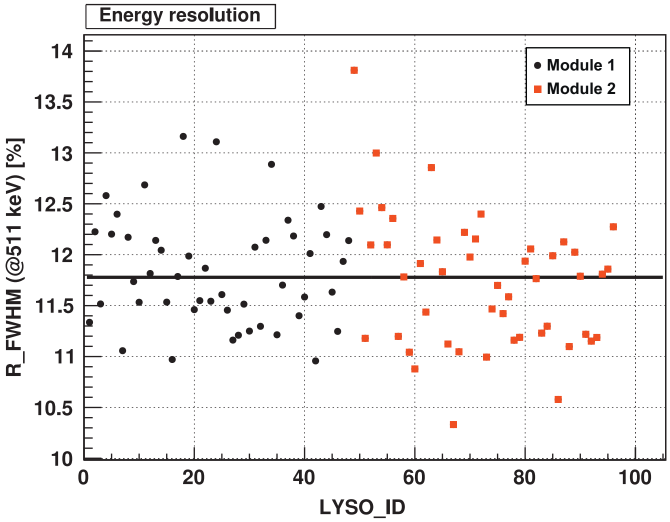

Fig. 18. Energy resolution (FWHM) at 511 keV for each crystal of the two AX-PET modules.

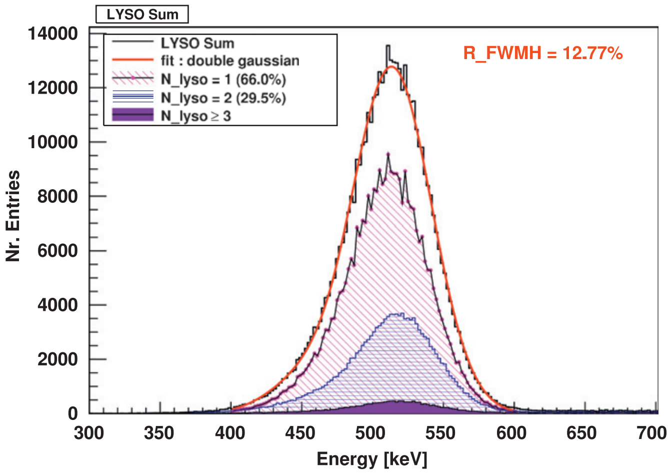

Fig. 19. Summed energy distribution in one AX-PET module exposed to 511 keV photons from the ^{22}Na source. The double Gaussian fitting function (bold red line) is required to properly describe the photopeak and the Lu X-ray escape peak. Also shown are the contributions to the total energy sum from different multiplicities of hit crystals (N_lyso = 1; N_lyso = 2; N_lyso ≥ 3). (For interpretation of the references to color in this figure legend, the reader is referred to the web version of this article.)

In Fig. 18 a mean energy resolution of 11.8% (FWHM) at 511 keV – averaged over the 96 crystals of both modules – is demonstrated; a good uniformity among different crystals is also observed.

Compatible results are obtained also from the event by event energy sum distribution in Fig. 19, where an energy resolution of 12.8% (FWHM) at 511 keV is obtained. It should be noticed that this sum distribution is not the histogram of the hardware analog sum of the module; it is instead the sum of the energies of all the hits recorded for each event. The small uncertainties deriving from the calibration procedure are responsible for the worsening of the energy resolution on the sum, when compared with the single crystal average resolution. On the other hand, the energy sum distribution manifests the correct functioning of the external trigger, with its high energy discrimination on the module energy sum. The distribution is fitted with the sum of two Gaussian functions, which represent the photopeak and the Lu X-ray escape peak. This latter one – not resolvable as a separate peak – is the reason for the asymmetric shape of the summed energy distribution. On the same plot, the relative contribution to the sum from the different multiplicities of hit crystals is also shown.

4.7. Path length dependence of the light yield

The absorption of the scintillation light during its propagation through the length of the LYSO crystal is studied. As an option in the analysis, data could be corrected by this effect. A scan along the Z direction with a collimated beam centered on one LYSO crystal shows the measured energy versus the axial position, as seen in Fig. 20. Similarly to the energy calibration, the procedure is repeated individually for each crystal. The behavior is independently parametrized with a suitable fitting function:

$$E(z) = N\left(e^{-z/\lambda^*_{opt}} + Re^{-(2L-z)/\lambda^*_{opt}}\right) \tag{3}$$

where λ^*_{opt}, R and N represent, respectively, the effective optical attenuation length, the reflectivity of the mirror coating (opposite to the photodetector) and a normalization factor. L is the length of the crystal bar, equal to 10 cm. As shown in the figure, a fit in which the reflectivity is constrained to be smaller than 90% does not reproduce well the data. When all the fit parameters λ^*_{opt},R,N are left free, an unphysical value for the reflectivity (>1) and a significantly reduced attenuation length are found. This indicates that the absorption mechanism cannot be described with a single absorption phenomenon, as proposed in Eq. (3), but there are other factors contributing to it, such as effects related with the side-by-side assembling of the crystals in the matrix, or a diffuse reflection component at the evaporated metal surface. When the LYSO data are corrected by the optical attenuation length, by extrapolating to the value $E(Z=0)$, an improvement of 0.15% is obtained on the energy resolution of the LYSO energy sum (from 12.77% to 12.62%).

A similar study is performed for the optical attenuation length of the light propagation inside the WLS strips (Fig. 21). Here, a simple exponential fit is used to describe the pathlength dependence of the light yield:

$$E(z) = Ne^{-y/(\lambda^*_{opt})_{WLS}}. \tag{4}$$

When the WLS strips raw data are corrected for the attenuation and their response equalized, a better uniformity is achieved.

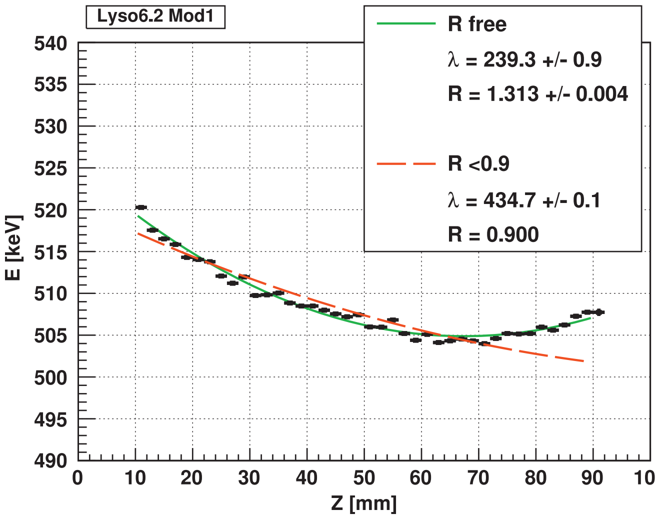

Fig. 20. Apparent energy deposition in one LYSO crystal versus the distance of the photon interaction point from the photodetector, for photoelectric absorption events, after the energy calibration. Also shown are two fitting curves, as in Eq. (3) for $R \leq 0.9$ (red dashed line) and R free (continuous green line). (For interpretation of the references to color in this figure legend, the reader is referred to the web version of this article.)

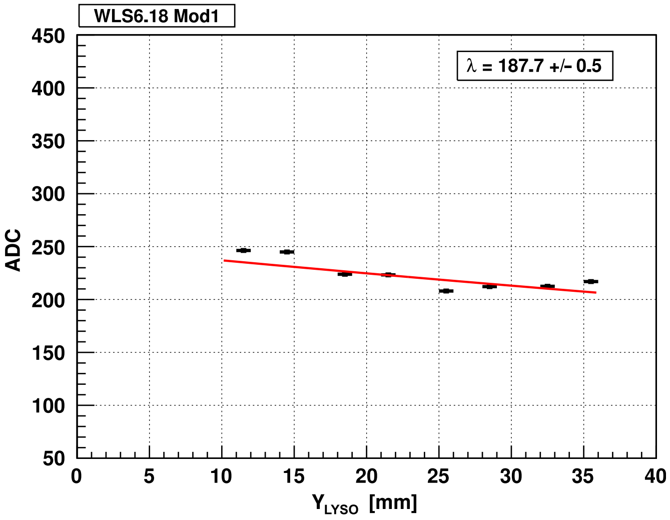

Fig. 21. Apparent light yield of one WLS strip versus the distance from the photodetector for photoelectric absorption events. The assigned Y coordinate is the center of the detected crystal. The WLS strip is selected as the strip corresponding to the center of gravity of the cluster.

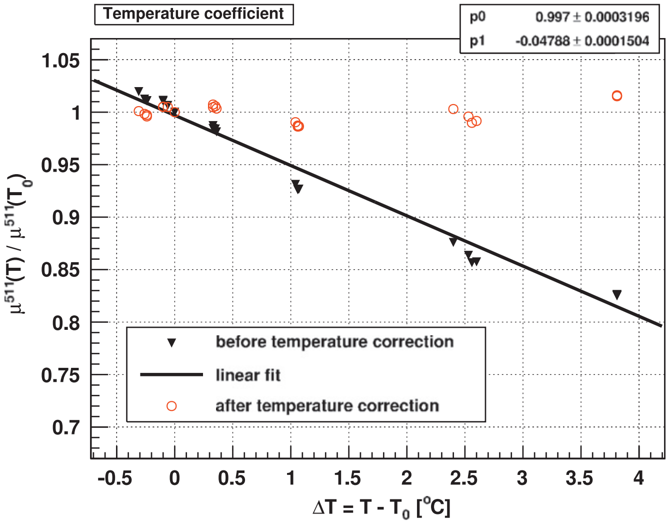

Fig. 22. Positions of the 511 keV peak as a function of the temperature variation, for a long time sequence of identical repeated runs. The plot shows both raw and corrected data.

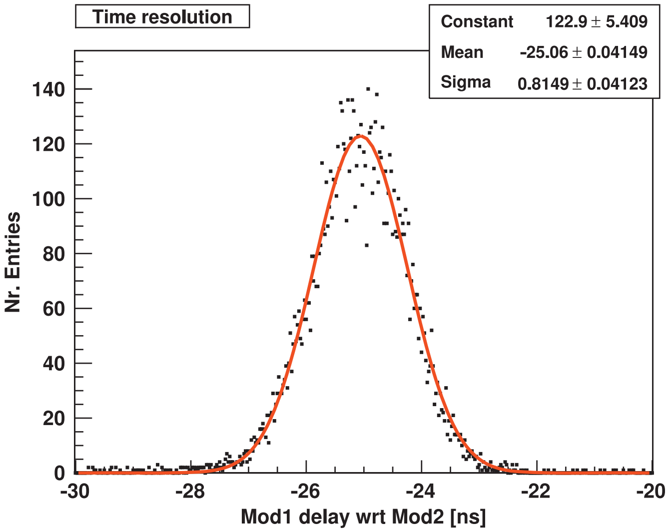

Fig. 23. Relative timing of one module versus the other, when the two modules are used in coincidence. In details the plot shows the delay of the discriminated summed signal of one module (LL × HL × $\overline{\text{HHL}}$) versus the coincidence signal of the two modules.

The improvement on the achieved spatial resolution is, however, only minimal.

4.8. Temperature correction coefficient

As explained, the bias for the MPPCs is adjusted according to the temperature recorded at the beginning of each run. For long data acquisitions periods (e.g. a scan with several consecutive runs) this would, however, be unpractical and time consuming. The bias is then adjusted only at beginning of the acquisition (at T_0 temperature) and the recorded ADC values are then corrected offline, using the measured temperature variations $\Delta T = T - T_0$. The temperature coefficient $\alpha = dG/dT$ has been extracted directly from the data (Fig. 22), by dedicated repeated measurements performed with identical experimental conditions, while varying the temperatures. For those runs, the bias has been adjusted initially (for $T = T_0$) and the position of the photopeak has been taken as a reference. The measurements confirm that the gain varies linearly with the temperature over a large temperature range. The temperature correction coefficient is $\alpha = dG/dT = -4.8\%/\,\mathrm{K}$ (data points before correction). The offline correction on the data is performed as follows:

$$ADC^{corr}(T) = ADC^{meas}(T)(1+\alpha\Delta T)^{-1}. \qquad (5)$$

The proper functioning of the correction procedure over the full temperature range can be seen from the data points after correction.

5. Coincidence measurements

When the two modules are used in coincidence, complementary information on the module performance concerning time and spatial resolution are achieved.

5.1. Time resolution

The AX-PET readout does not provide any time information on individual channels. Dedicated timing measurements are performed using a Lecroy Waverunner LT584, 1 GHz oscilloscope, and acquiring the relative delay between the discriminated outputs of the modules summed signals (LL × HL × $\overline{\text{HHL}}$). The measured time jitter between the two modules is shown in Fig. 23. A time resolution of about 800 ps is achieved, measured as the standard deviation of the time-difference curve. This includes contributions from the LYSO scintillation decay time, from the propagation time of the photons though the crystals and from the front-end and trigger electronics. The achieved time resolution would allow for a small coincidence window of a few nanoseconds between the two modules, which would minimize the contribution of accidental triggers. However, the current AX-PET electronics requires a minimum pulse width for the trigger and the data lock of about 60 ns. This prevents the system to fully profit of its time performance, especially for rejection of accidentals.

5.2. Focal plane reconstruction

With the two modules used in coincidence, a simple bi-dimensional geometrical reconstruction of the source position is achieved, with the intersection of all the detected lines of response (LOR). For this purpose, only the photoelectric events in both modules are selected (~44% of the total statistics) and the coordinates of the interaction points are defined for each of the two modules, in the usual way. The transaxial (*X*,*Y*) coordinate is assigned at the center of the LYSO crystal (discrete variable), the axial *Z* coordinate is computed from the center of gravity method on the WLS cluster (continuous variable). For each event, a line connecting the two interaction points is drawn, both in the *XY* and in the *XZ* projection planes (Fig. 24). The intersection of those LORs with the middle planes ($X=0$) determines the bi-dimensional geometrical reconstruction of the source, in the axial and in the transaxial direction (Figs. 25 and 26).

5.3. Axial resolution

A Gaussian fit applied to the *Z* distribution of the LOR intersection with the focal plane (Fig. 25) gives an indication of the achieved axial resolution of the system. The fitted σ value includes contributions from the intrinsic resolutions of the two modules, the finite positron range and the non-collinearity of the emitted photons (for a distance between the modules of 150 mm). When the contribution from the e^+ annihilation physics is subtracted, an intrinsic axial resolution of 1.34 mm (FWHM) is obtained. Comparing with the resolution of the single

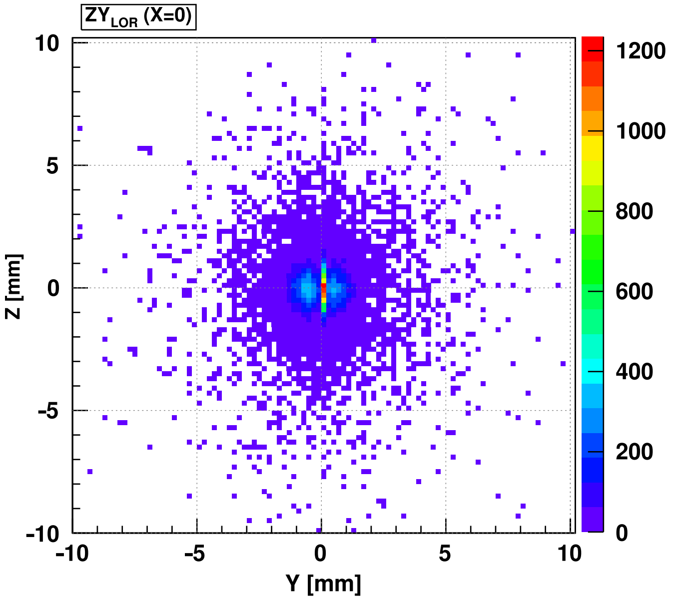

Fig. 26. Focal plane reconstruction of the ^{22}Na source in the plane $X=0$, obtained from the intersection of the all the detected LOR in the middle plane. The continuous (*Z*–vertical) and discrete (*Y*–horizontal) nature of the two distributions can be observed.

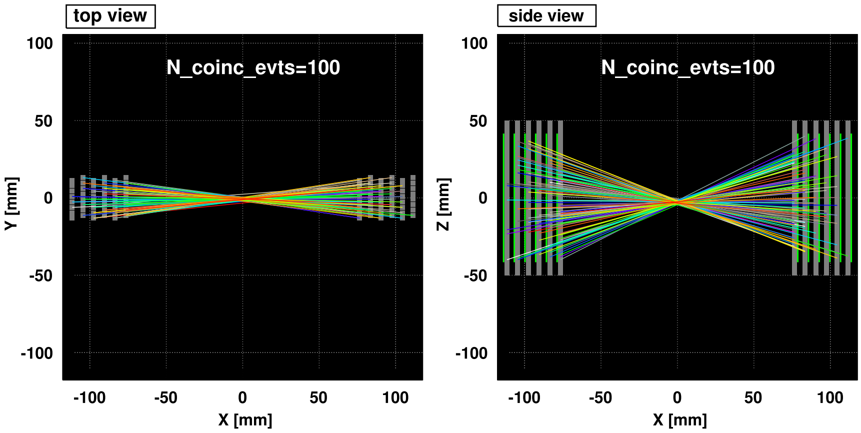

Fig. 24. Drawing of the lines of response of 100 coincidence events, both on the transaxial *XY* plane and on the axial *XZ* plane. Only photoelectric absorption events, with one and only one good cluster, are considered. The ^{22}Na source is placed between the two modules, at the nominal coordinates origin (0,0,0). The modules geometry and distances are shown. The distance between the modules is 150 mm.

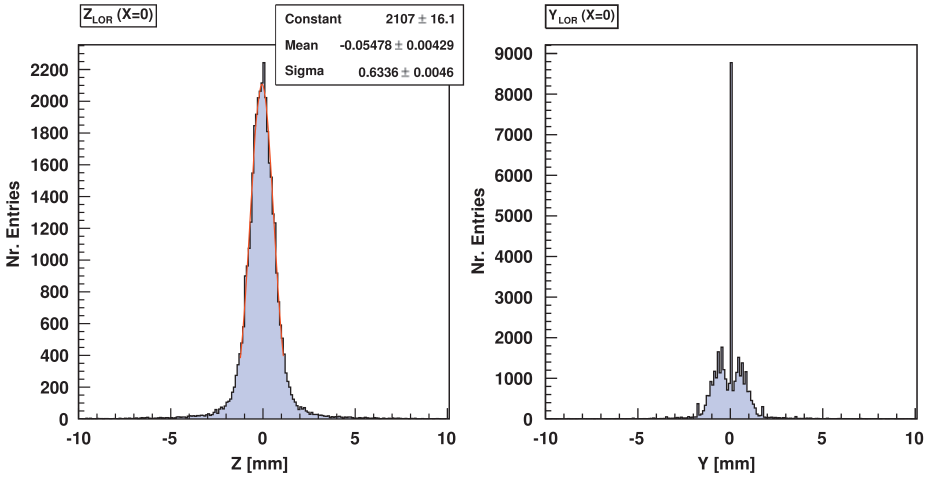

Fig. 25. Intersection of the lines of response with the central plane ($X=0$), where the ^{22}Na source is placed. The projections on the two axes (*Z* and *Y*) are individually shown. The spikes observed in the *Y* projection, with a 1.75 mm pitch, arise from the discrete nature of the interaction points (center of crystals) in the *XY* plane.

detector modules ($\sim$ 1.8 mm, see Section 4.3), the expected improvement by a factor $1/\sqrt{2}$ is observed.

6. Conclusions and outlook

The present paper describes the AX-PET demonstrator, consisting of two identical camera modules used in coincidence. The demonstrator represents a fully operational implementation of the Axial PET concept, based on long axially oriented crystal bars and orthogonal WLS strip arrays. The two modules of the demonstrator have been fully characterized in terms of sensitivity, uniformity, spatial resolution and energy resolution, using point-like radioactive ^{22}Na sources. For the measurements described, the analysis has been restricted to photoelectric absorption events. Additional corrections (energy calibration and pathlength dependence of the light yield) have also been included for a better understanding of the detector. These corrections will be essential when events involving Compton interactions in the crystal matrices will also be included. The methods and the results of the characterization measurements have been detailed in the paper. The performance figures obtained with the AX-PET demonstrator confirm the axial concept as a highly competitive alternative to standard geometries.

In the meantime, the demonstrator set-up has been further characterized in a real PET coincidence configuration, employing point-like sources and phantoms of increasing complexity (capillaries, cylinders, micro-Derenzo and NEMA) filled with standard ^{18}F-based fluorodeoxyglucose (FDG) radiotracer. The available two modules allow only a very incomplete ring coverage. This is compensated by rotating the source arrangement or phantom. Details of the dedicated reconstruction code and the tomographic images of the phantoms which are currently being reconstructed will be published in forthcoming articles.

Acknowledgments

The construction and characterization of the AX-PET modules was only possible thanks to the help of many competent technicians. We would like to acknowledge the contributions of C. David, A. Folley, N. Dixon, P. Lancon, and B. Cantin at CERN, as well as M. Dröge, C. Haller and U. Horisberger from ETH Zurich. We are grateful to A. Kehrli (CERN) for the excellent support of the movement control software; V. Commichau and H. von Gunten (ETH Zurich) for the entire development of the MPPC bias control system; M. Joos and N. De Metz-Noblat (CERN) for their precious help in setting up the DAQ system based on MEN A20 VME controller. The work is partially funded through the Spanish Ministry of Science & Innovation under Grant FPA2008-02419-E and project Grant TEC2007-61047. P. Solevi is supported by the Marie Curie Intra-European Fellowship Grant 237620 for the project INSPET. P. Beltrame is supported through the Marie Curie Initial Training Network MC-PAD (GA no. 214560-2).

References

[1] M. Blume, et al., IEEE Trans. Med. Imaging 29 (11) (2010) 1892.
[2] 〈https://cern.ch/twiki/bin/view/AXIALPET〉.
[3] M. Rafecas, et al., Phys. Med. Biol. 48 (7) (2003) 821.
[4] K. Shimizu, et al., IEEE Trans. Nucl. Sci. NS-34 (1) (1988) 717.
[5] J. Séguinot, et al., Il Nuovo Cimento C 29 (2005) 429.
[6] F. Ciocia, et al., Nucl. Instr. and Meth. A 600 (2009) 506.
[7] A. Braem, et al., Nucl. Instr. and Meth. A 586 (2008) 300.
[8] E. Bolle, et al., Nucl. Phys. B (Proc. Suppl.) 197 (2009) 19.
[9] A. Braem, et al., Nucl. Instr. and Meth. A 610 (2009) 192.
[10] V. Commichau, et al., A multi-channel G-APD bias voltage supply based on the AD5535 32 channel DAC circuit ETH Zurich, Institute for Particle Physics Technical Note, 2010, ETHZ-IPP-2010-06.
[11] E. Chesi, et al., Nucl. Instr. and Meth. A 564 (2006) 352.
[12] R. Brun, F. Rademakers, Nucl. Instr. and Meth. A 389 (1997) 81. (see also 〈http://root.cern.ch/〉).
[13] P. Beltrame, et al., Nucl. Instr. and Meth. A 628 (2011) 426.
[14] P. Solevi, et al., in: Proceedings of the SPIE 2011 Medical Imaging Conference, to be published.
[15] Center for X-Ray Optics, X-Ray Data Booklet LBNL/Pub-490 Rev. 3, 2009.
[16] E. Chesi, et al., Contribution to the WLS studies for the Axial PET, CERN Technical Note, 2010, PH-EP-Tech-Note-2010-014.
[17] S.E. Derenzo, et al., Critical instrumentation issues for 2 mm resolution, high sensitivity brain PET, in: K. Uemura, N.A. Lassen, T. Jones (Eds.), Published in Quantification of Brain FunctionElsevier Science Publishers, 1993, pp. 25–37.
[18] K. Komura, et al., Nucl. Phys. A 198 (1972) 73.